High-performance Bifunctional hollow structures Cobalt-based Phosphides Catalysts for Water Splitting

Wei Zhang[1†], Ning Han[1†], Jiangshui Luo*[2], Wei Guo[1], Sijie Xie[1], Zhenyu Zhou[1] , Palaniappan Subramanian[1], Kai Wan[1], Xu Han[3], Jordi Arbiol[3,4], Chi Zhang*[5], Maowen Xu[6], Xuan Zhang*[1] and Jan Fransaer*[1]

1 Department of Materials Engineering, KU Leuven, Leuven, 3001 Belgium.

2 College of Materials Science and Engineering, Sichuan University, Chengdu, 610065 P.R. China.

3 Catalan Institute of Nanoscience and Nanotechnology (ICN2), CSIC and BIST, Campus UAB, Bellaterra, 08193 Barcelona, Catalonia, Spain

4 ICREA, Pg. Lluís Companys 23, 08010 Barcelona, Catalonia, Spain

5 School of Applied Physics and Materials, Wuyi University, Jiangmen, 529020 P.R. China.

6 Key Laboratory of Luminescent and Real-Time Analytical Chemistry, Ministry of Education, School of Materials and Energy, Southwest University, Chongqing 400715, P. R. China.

† W. Z. and N.H. contributed equally to this work.

* Corresponding authors.

E-mail addresses: jiangshui.luo@scu.edu.cn (J. L); chizhang@wyu.edu.cn (C. Z); xuan.zhang@kuleuven.be (X. Z); jan.fransaer@kuleuven.be (J. F)

Abstract

Cobalt phosphides electrocatalysts have great potential for water splitting, but the unclear active sides hinder the further development of cobalt phosphides. Wherein, cobalt phosphides hollow structure (CoP-HS, CoP_2-HS and CoP_3-HS) catalysts based on same sacrificial template were prepared. Surprisingly, these cobalt phosphides exhibited similar OER but quite different HER performances. The identical OER performance of these CoP_x-HS in alkaline solution were attributed to the similar surface reconstruction to CoOOH. CoP-HS exhibited the best catalytic activity for HER among these CoP_x-HS, originating from the adjusted electronic density of phosphorus to affect absorption-desorption process on H. Moreover, CoP-HS displayed good performance (cell voltage of 1.47 V at a current density of 10 mA cm^{-2}) and high stability in 1 M KOH. This work could provide the guidance for the future investigations on transition metal phosphides for water splitting from material design to mechanism understanding.

1. Introduction

Hydrogen will almost certainly play a role in future renewable energy plans.[1,2] Generation of hydrogen by sustainable electrochemical processes form water is an appealing strategy.[3,4] Electrochemical water splitting involves two reactions: the cathodic hydrogen evolution reaction (HER) and the anodic oxygen evolution reaction (OER). Presently, platinum (Pt) and noble metal oxides, including ruthenium dioxide (RuO_2) and iridium dioxide (IrO_2), are the state-of-the-art electrocatalysts to drive HER and OER, respectively.[5] Nevertheless, the scarcity and associated high costs of these noble metals severely restrict their large scale application.[6] Hence, the lower product cost, tolerance of catalysts working conditions for both reactions, the development of bifunctional catalysts, free from Pt-group metals, has gained increasing attention.[7,8,9]

Different transition metal-based catalysts have been explored as bifunctional catalysts for electrochemical water splitting, such as oxides, hydroxides, borides, selenides, nitrides and so on.[10,11,12,13] Among these nonprecious metal electrocatalysts, transition metal phosphides (TMPs) are considered as the promising alternatives catalyst for both HER and OER. In particular, cobalt phosphides have attracted the most attention due to their high catalytic activity and durability in alkaline solution.[14] For instance, Yoo and co-workers reported that porous CoP nanoparticles exhibit good HER and OER activities owing to the increase of the accessible catalytic active sites.[15] However, the poor conductivity, unclear active sides and low reaction kinetics hinder the practical use of cobalt phosphides.

58   To further improve electrochemical performance of TMPs, two approaches have

59   been proposed: (1) Rational design of nanostructures to increase the number of

60   exposed active sites and promote ion transport, such as nanoneedle, nanosheet,

61   core-shell and hollow nanostructure.[16,17,18,19] Among those, hollow nanostructured

62   catalysts materials have attracted a lot of research interests, because the high

63   surface-to-volume ratio, low density and small transmission lengths of mass and

64   charge.[20] For example, compared with Ni–Co–P nanosheets, the Ni–Co–P hollow

65   nanobricks are demonstrated as the more efficient bifunctional electrocatalysts for

66   overall water splitting with a potential of 1.62 V to reach the current density of 10 mA

67   cm^{-2}.[21] (2) Understanding of active sites in cobalt phosphides. The mechanism of

68   water splitting on cobalt phosphides is still under debate due to the complicate phase

69   and structure change and unclear active sites. Some studies announced that the cobalt

70   phosphides are stable during OER cycling.[22,23,24] Others believe that cobalt

71   phosphides transform to oxide/oxyhydroxide during OER.[25] Besides, cobalt

72   phosphides have various stoichiometries, such as Co_2P, CoP, CoP_2 and CoP_3.

73   In this work, based on the same ZIF-67 sacrificial template, a series of cobalt

74   phosphides with a similar, hollow morphology were synthesized. The resulting

75   catalyst exhibits similar nanocages with a porous structure. Interestingly, the different

76   cobalt phosphides showed similar OER performance but different HER performance.

77   In-depth structural characterizations and electrochemical studies show that the

78   different cobalt phosphides convert during OER to the active catalyst. After cycling in

79   alkaline solution, the active surface for all catalysts becomes oxyhydroxide which had

4

80   a similar activity with an overpotential of 270~280 mV at a current density of 10 mA

81   cm^{-2} for OER. On the contrary, all the cobalt phosphides with hollow structures

82   remained stability during HER test. Among these catalysts, CoP-HS nanocages

83   showed the best catalytic activity for HER with an overpotential of -116 mV which

84   could be the catalytically active sites for HER at a current density of -10 mA cm^{-2} in 1

85   M KOH. Density functional theory (DFT) computation revealed that the P-sites in

86   CoP_x-HS are the primary catalytically active site for HER, and the calculated ΔG_{H*}

87   based on P-sites of CoP-HS agrees well with the corresponding normalized HER

88   performances. When CoP-HS//CoP-HS were used for water splitting, a current

89   density of 10 mA cm^{-2} is achieved at a remarkably low cell voltage of 1.47 V, which is

90   due to the hollow structure of the catalysts and the high activity of the P-sites in CoP.
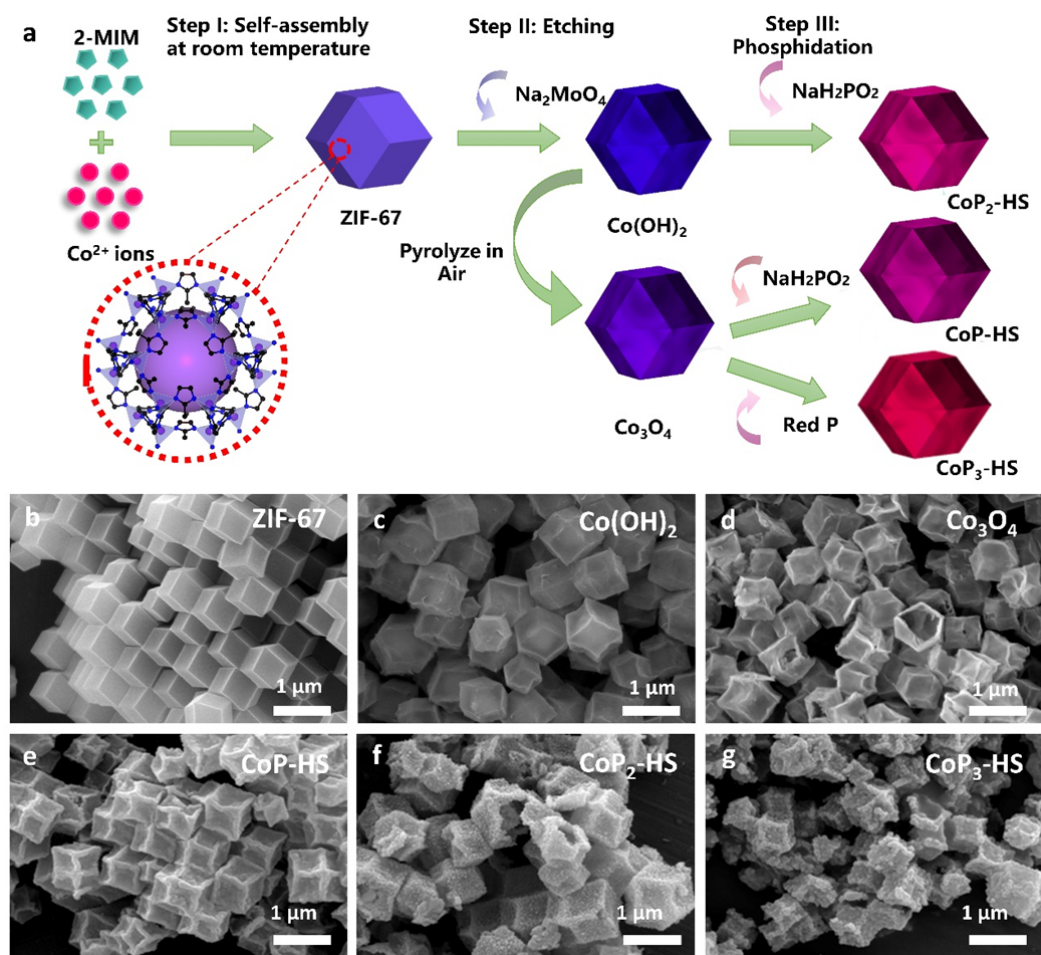
2. Results and discussion

Figure 1. (a) Schematic illustration of the synthesis process of hollow cobalt phosphides nanocages. SEM images of pure ZIF-67 **(b),** $Co(OH)_2$ **(c)**, Co_3O_4 **(d),** CoP-HS **(e),** CoP_2-HS **(f)** and CoP_3-HS **(g).**

The synthesis process of the three different cobalt phosphides nanocages are shown in **Figure 1a**. In order to ensure the same morphology for all CoP_x catalysts were synthesized based on the same ZIF-67 sacrificial template. The rhombic dodecahedral ZIF-67 particles are shown in **Figure S1a**. Next, the ZIF-67 particles were converted into hollow $Co(OH)_2$ structures by the reaction of with an aqueous

101   Na_2MoO_4 solution based on the Kirkendall effect.[26,27] Co_3O_4 nanocages were

102   fabricated by annealing the hollow $Co(OH)_2$ particles at 500 ºC in air. Subsequently,

103   the hollow $Co(OH)_2$ and Co_3O_4 particles were annealed together with NaH_2PO_2 in N_2

104   atmosphere together at 700 ºC, resulting in the formation of hollow CoP_2 particles

105   (named CoP_2-HS) and hollow CoP particles (named CoP-HS), respectively. Hollow

106   CoP_3 particles (named CoP_3-HS) was prepared by annealing Co_3O_4 particles with red

107   phosphorus in N_2 at 700 ºC. As shown in **Figure 1b**, the prepared rhombic

108   dodecahedron shape ZIF-67 particles exhibited a uniform particle size of

109   approximately 800 nm and perfectly flat facets. The X-ray diffraction (XRD) pattern

110   of ZIF-67 matched well with the simulated pattern (**Figure S1a**), which demonstrates

111   the purity of the starting phase. It clearly shows that during these transformations, the

112   initial morphology and particle size of ZIF-67 is preserved (**Figure 1c&1d**). Because

113   the structure was transformed from solid to hollow, the surface of the $Co(OH)_2$ and

114   Co_3O_4 nanocages becomes wrinkled and protuberance-like. The formation of hollow

115   structure of $Co(OH)_2$ and Co_3O_4 can be identified from several broken samples. XRD

116   pattern presented in **Figure S1b** shows the presence of both α-$Co(OH)_2$ and

117   β-$Co(OH)_2$ in the prepared $Co(OH)_2$. As shown in **Figure S1c**, the diffraction pattern

118   of the Co_3O_4 is in good agreement with the standard pattern of Co_3O_4 (JCPDS 1-1152)

119   powder. The uniform distribution of Co and P in the synthesized Co_3O_4 was proven by

120   the energy-dispersive X-ray (EDX) (**Figure S2**). After phosphidation, the three cobalt

121   phosphides have the original polyhedron shape of the ZIF-67 precursor. The diameters

122   of these particles are in the range of 600 to 800 nm. As shown in **Figure S3**, the

7

123 overlap of P and Co elements in SEM-EDS mapping confirms the homogeneous

124 formation of all three cobalt phosphides (CoP-HS, CoP₂-HS, and CoP₃-HS).

125
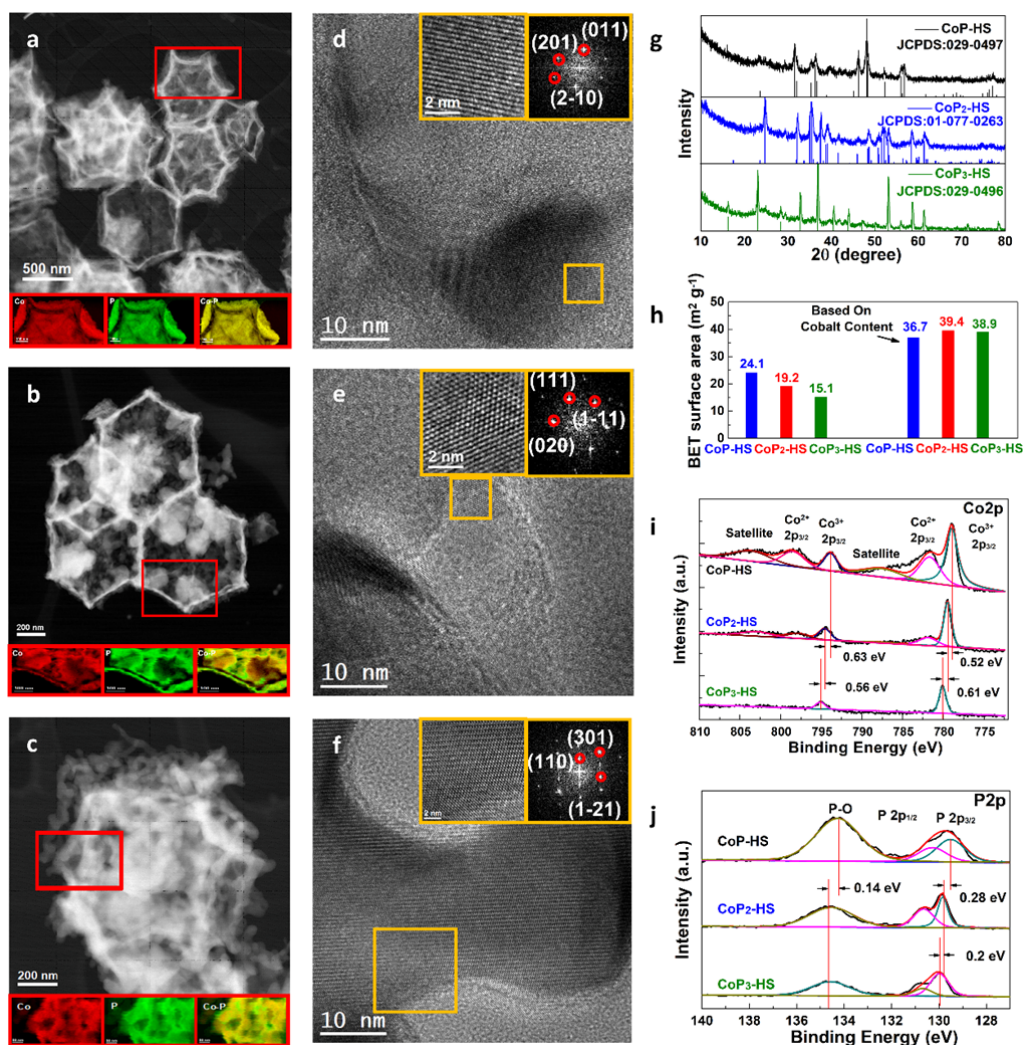
Figure 2. TEM images of CoP-HS **(a)**, CoP₂-HS **(b)** and CoP₃-HS **(c)**. EELS chemical composition maps of CoP-HS **(a)**, CoP₂-HS **(b)** and CoP₃-HS **(c)** obtained from area inside the red square on the HAADF STEM micrograph. Individual Co L2,3-edges at 779 eV (red), P L2,3-edges at 132 eV (green) and composite of Co-P. HRTEM images and corresponding indexed power spectra (FFT) of CoP-HS showing a CoP orthorhombic crystal with Pnma phase along its [12-2] axis **(d),** CoP₂-HS showing a CoP₂ monoclinic crystal with P2₁/C phase along its [10-1] axis **(e)** and CoP₃-HS showing a CoP₃ cubic crystal with Im3 phase along its [-113] axis **(f)**. **(h)** BET surface area of CoP-HS, CoP₂-HS and CoP₃-HS based on cobalt content. **(g)** XRD patterns of

8

134 CoP-HS, CoP$_2$-HS $_s$and CoP$_3$-HS. XPS spectra of Co 2p **(i)** and P 2p **(j)** for CoP-HS, CoP$_2$-HS and

135 CoP$_3$-HS.

136   The well-defined nanocage-shaped structure and particle sizes (range from 600

137 nm to 800 nm) of the three cobalt phosphides are also confirmed by transmission

138 electron microscopy (TEM) images (**Figure 2**). The EELS chemical composition

139 maps of the three cobalt phosphides were obtained from the region inside the red

140 square in the HAADF STEM micrograph, shown in **Figure 2a-c,** for CoP-HS,

141 CoP$_2$-HS, and CoP$_3$-HS, respectively. As can be seen in these maps, Co and P are

142 uniformly distributed in the selected nanostructure. But the P signal is stronger in

143 CoP$_2$-HS and CoP$_3$-HS. A HRTEM micrograph was taken from the nanoparticle

144 inside the orange square (**Figure 2d**). Details of this region and its corresponding

145 power spectrum reveals that this nanoparticle has a crystal phase that is in agreement

146 with the CoP-HS orthorhombic phase (space group = Pnma) with a=5.0760 Å,

147 b=3.2770 Å and c=5.5990 Å. From the crystalline domain in **Figure 2d**, the CoP-HS

148 lattice fringe distances are 0.286 nm, 0.237 nm, and 0.199 nm, at 78.95º and 122.43º

149 which correspond to the orthorhombic CoP phase, visualized along its [12-2] zone

150 axis. For the CoP$_2$-HS sample, a HRTEM micrograph was taken from the nanoparticle

151 inside the orange square (**Figure 2e**). Details of this region and its corresponding

152 power spectrum, reveals that this nanoparticle has a crystal phase that is in agreement

153 with the CoP$_2$-HS monoclinic phase (space group = P21/C) with a=5.5510 Å,

154 b=5.5490 Å and c=5.6140 Å. From the crystalline domain in **Figure 2e**, the CoP$_2$-HS

155 lattice fringe distances are 0.277 nm, 0.272 nm, and 0.281 nm, at 60.83º and 121.60º

156   which correspond to the monoclinic CoP_2-HS phase, visualized along its [10-1] zone

157   axis. As illustrated in **Figure 2f**, the CoP_3-HS cubic phase (space group = Im3) with

158   a=b=c=7.7112 Å can be proven from the corresponding power spectrum from a

159   HRTEM micrograph taken from the nanoparticle inside the orange square. The

160   CoP_3-HS lattice fringe distances (**Figure 2f**) are 0.553 nm, 0.243 nm, 0.313 nm and

161   0.313 nm, at 46.97º, 72.21º and 106.50º which could be interpreted as the cubic

162   CoP_3-HS phase, visualized along its [-113] zone axis.

163   The crystalline structures and successful phosphidation process of these samples

164   are also confirmed by the XRD (**Figures 2g**). The experimental XRD patterns match

165   well with corresponding standard three cobalt phosphide crystal structures (ICDD

166   PDF: 029-0497 for CoP-HS, ICDD PDF: 01-077-0263 for CoP_2-HS and ICDD PDF:

167   029-0496 for CoP_3-HS) without unidentified peaks. These results indicate that the

168    $Co(OH)_2$ and Co_3O_4 were completely converted into the intended cobalt phosphides.

169   The Brunauer-Emmett-Teller (BET) specific surface area and pore size distributions

170   of the as-synthesized three cobalt phosphides were determined by N_2 sorption

171   experiments. The N_2 adsorption-desorption isotherms and Barrett-Joyner-Halenda

172   (BJH) pore-size distribution of CoP-HS, CoP_2-HS and CoP_3-HS nanocages are shown

173   in **Figure S4**. All of the cobalt phosphides show a type-IV isotherm loop, which

174   indicates the mesoporous characteristics of the materials. For the three cobalt

175   phosphides, the major pore size distributions are displayed at a region of 1.5 to 3.0 nm.

176   Moreover, BET surface areas of CoP-HS, CoP_2-HS and CoP_3-HS are 24.1, 19.2 and

177   15.1 m^2 g^{-1} (**Figure 2h**), respectively. With increasing phosphorus content, the

178   specific surface area decreased. Interestingly, after normalizing the specific surface

179   areas to the mass of cobalt, the normalized specific surface areas of all three cobalt

180   phosphides are similar (**Figure 2h**). This phenomenon can be explained by the same

181   self-sacrificing template was used. All these results prove that the successful synthesis

182   of three different cobalt phosphides (CoP-HS, CoP_2-HS and CoP_3-HS) with similar

183   structure and morphology by the presented top-down strategy.

184   X-ray photoelectron spectroscopy (XPS) is used for the analysis of chemical

185   state and the overall electronic structure of these catalysts. As shown in **Figure S5**, the

186   XPS survey spectrums of three cobalt phosphides reveal the existence of Co and P.

187   The Co 2p spectra of the CoP-HS (**Figure 2i**) is deconvoluted into six peaks, which

188   binding energies located at 778.9, 793.8, 787.6 eV that can be assigned to Co $2p_{3/2}$,

189   and binding energies located at 781.7, 798.5, 803.8 eV that can be assigned to Co $2p_{1/2}$.

190   Among them, the peaks centered at 787.6 and 803.8 eV are the satellite peaks of $2p_{2/3}$

191   and $2p_{1/2}$, respectively. The binding energy at 778.9 and 793.8 eV can be attributed to

192   Co^{3+}, and those located at 781.7 and 798.5 eV belong to Co^{2+}. Compared with CoP,

193   the Co 2p peaks in CoP_2-HS and CoP_3-HS shifted to a higher binding energy. The

194   main reason of this shift is due to the higher P content in CoP_2-HS and CoP_3-HS. A

195   higher concentration of electronegative phosphorus shifts the peaks of Co^{3+} to higher

196   binding energies. In addition, compared to the Co^{2+} peaks in the three cobalt

197   phosphides, there is a gradual decrease in the peak intensities from CoP-HS to

198   CoP_3-HS. In the P 2p spectrum of CoP-HS (**Figure 2j**), the peaks located at 129.5,

199   130.3 and 134.2 eV are indexed to P $2p_{3/2}$, P $2p_{1/2}$ in cobalt phosphide and surface

200   oxidation of P, respectively.[28] Compared with CoP$_3$-HS, the peaks of CoP-HS and

201   CoP$_2$-HS in P 2p$_{3/2}$, P 2p$_{1/2}$ region shifted to lower binding energy. The negative shift

202   of P 2p binding energy, induced by changing cobalt-phosphorus composition, shows

203   the enhanced electron occupation, which can give rise to the improvement of the

204   electron-donating ability of the catalyst.[29]

205
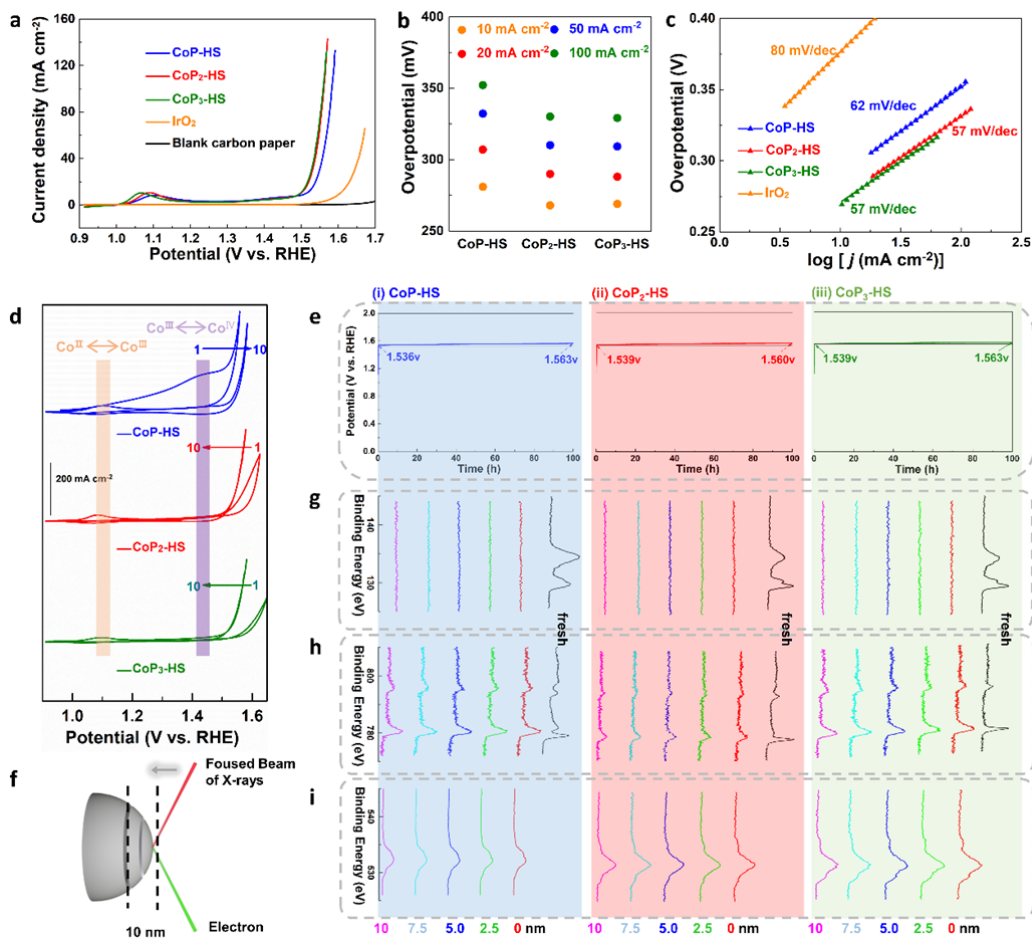
206   **Figure 3. (a)** The LSV curves of CoP-HS, CoP$_2$-HS, CoP$_3$-HS, IrO$_2$ and carbon paper measured in

207   1.0 M KOH solution toward OER at a scan rate 10 mV/s after activation by 50 CV cycles between

208   0.0 V and 0.85 V (vs. Hg/HgO) at a scan rate 50 mV/s. **(b)** The data of CoP-HS, CoP$_2$-HS and

209   CoP$_3$-HS at different current density. **(c)** The corresponding Tafel plots for the samples. **(d)** The

210   CV curves obtained at the 1st and 10th cycles at a scan rate of 10 mV/s in a 1.0 M KOH solution.

211   **(e)** The potential of CoP-HS, CoP$_2$-HS and CoP$_3$-HS versus time at a current density of 20 mA

212 cm^{-2} in 1.0 MKOH. (All the tests were taken on carbon paper). **(f)** The schematic of surface

213 composition investigation via XPS in different depths after ion beam etching. **(g)** High-resolution

214 P 2p XPS spectra of the fresh CoP-HS, fresh CoP$_2$-HS, fresh CoP$_3$-HS and post-OER samples. **(h)**

215 High-resolution Co 2p XPS spectra of fresh CoP-HS, fresh CoP$_2$-HS, fresh CoP$_3$-HS and

216 post-OER sample. **(i)** High-resolution O 1s XPS spectra of the post-OER CoP-HS, post-OER

217 CoP$_2$-HS and post-OER CoP$_3$-HS samples.

218   Cobalt based phosphides are considered as promising bifunctional catalysts for

219 both HER and OER. Firstly, the electrocatalytic OER performance of three cobalt

220 phosphides were examined in 1.0 M KOH using a three-electrode system and

221 different electrodes were prepared by coating carbon paper with approximately 1 mg

222 cm^{-2} of catalyst. The active site of cobalt based phosphides for OER is still on debate.

223 Even though, cobalt based phosphides have been reported as catalysts for OER,[23,24,30]

224 the structure and phase changes occurring during OER tests cannot be ignored. To

225 investigate the phase changes of three cobalt phosphides, the CV curves of three

226 cobalt phosphides at the 1st, 3rd, 5th, and 10th cycle were measured. As illustrated in

227 **Figure 3d&S6**, at the 1st cycle, the OER performance of CoP-HS seems better than

228 CoP$_2$-HS and CoP$_3$-HS, which could be explained by unstable of CoP$_x$-HS system.

229 Furthermore, as the number of cycles increases, the OER performance of CoP$_2$-HS

230 and CoP$_3$-HS improves, while the OER performance of CoP-HS decreases. At the

231 10th cycle the CV curves of CoP-HS, CoP$_2$-HS and CoP$_3$-HS almost overlap.

232 Therefore, all catalysts were first activated by 50 CV cycles at a scan rate 50 mV/s

233 between 0.0 V and 0.85 V (vs. Hg/HgO). LSV with *iR*-correction are used for

234 evaluated the OER performances of these catalysts (**Figure 3a**). For the purpose of

235   comparison, The OER performances of commercial IrO_2 and bare carbon paper were

236   also investigated. As shown in **Figure 3a**, the CoP-HS requires an overpotential of

237   281 mV at a current density of 10 mA cm^{-2}. Similar performance of the CoP_2-HS and

238   CoP_3-HS catalysts can be achieved, which overpotentials of resp. 268 mV and 269

239   mV at a current density of 10 mA cm^{-2}. All these catalysts show better performance

240   than commercial IrO_2 (375 mV). Meanwhile, the bare carbon paper hardly shows any

241   electrocatalytic activity for OER even at high overpotential (**Figure 3a**). The

242   corresponding Tafel slopes are derived from plotting overpotential against log (j)

243   (**Figure 3c**). CoP_2-HS and CoP_3-HS exhibit a similar Tafel slope of 57~62 mV dec^{-1}.

244   The Tafel slope results suggest that CoP-HS, CoP_2-HS and CoP_3-HS have similar

245   charge transfer kinetics during OER. The electrochemical durability of the catalyst is

246   a key parameter for practical application. The electrocatalytic stability of different

247   cobalt phosphides electrodes were investigated by chronopotentiometry at a constant

248   current density of 20 mA cm^{-2} (**Figure 3e**). The chronopotentiometry curves show that,

249   after 100 h, the catalytic activity of CoP-HS, CoP_2-HS and CoP_3-HS dropped by

250   6.5 %, 6.0% and 7.7%, respectively. This result suggests a good electrochemical

251   stability of all three cobalt phosphides for the OER in alkaline solution. At the cycling

252   tests, the three cobalt phosphides prepared in this paper show almost identical results

253   (1.563 V for CoP-HS, 1.560 V for CoP_2-HS and 1.563 V for CoP_3-HS, vs. RHE),

254   which indicates that the P composition does not influence the OER performance of

255   cobalt based phosphides in an alkaline medium. This could be caused by the

256   oxidization of the similar structure of CoP-HS, CoP_2-HS and CoP_3-HS surface during

257　the OER test. After the OER electrochemical durability test, SEM and EDS

258　measurements were conducted to characterize the morphologies and surface

259　compositions of the three cobalt phosphides. The SEM images show that the

260　morphology and structure of three cobalt phosphides are reasonably retained after

261　OER durability test (**Figure S7a-c**). But the surface composition of three cobalt

262　phosphides changes showing a loss of phosphorous after long-term OER durability

263　test in an alkaline medium (**Figure S7d**). This result is consistent with previous

264　papers. Metal-based materials, such as metal chalcogenides, metal pnictides and metal

265　carbides, are partly or completely transformed to oxides or (oxy) hydroxides under

266　sufficiently extended periods during alkaline OER testing[22,31,32]. To further investigate

267　the post-OER electrodes, the XPS was used to analyze the electrodes. Combining a

268　sequence of ion gun etch cycles, more quantified vertical information and information

269　evolution with thicknesses was obtained by depth-profiling X-ray photoelectron

270　spectroscopy (**Figure 3f**). As shown in **Figure 3g**, the characteristic signals for

271　phosphorous almost completely disappears from the surface. As for cobalt, only two

272　broad peaks corresponding to oxidized cobalt species were observed on the surface

273　for all three cobalt phosphides after OER (**Figure 3h**), which is consistent with a

274　previous report on CoOOH.[33] To further validate the formation of CoOOH, the O/Co

275　peak area ratio of was calculated based on the XPS detection at the surface and the

276　result is about 2:1 (**Figure 3h&i**). Argon ion sputtering was applied to remove the

277　oxidized surface (2.5 nm/per step) of the three cobalt phosphides after OER and

278　measured again to observe the XPS signals of P 2p (**Figure 3g**), Co 2p (**Figure 3h**),

279 and O 1s (**Figure 3i**). However, XPS results remain unchanged, which indicate the

280 complete transformation of the near surface region of all three cobalt phosphides (the

281 active region) during OER durability test.   This explains the similar OER

282 performance after durability test. According to these results, the near surface region of

283 all three cobalt phosphides transform via self-reconstruction into CoOOH. Therefore,

284 P composition will not affect the OER performance in an alkaline medium. After the

285 conversion into CoOOH, these catalysts have comparable or better OER activity than

286 reported metal-based phosphides electrocatalysts as shown in **Table S1**.

287
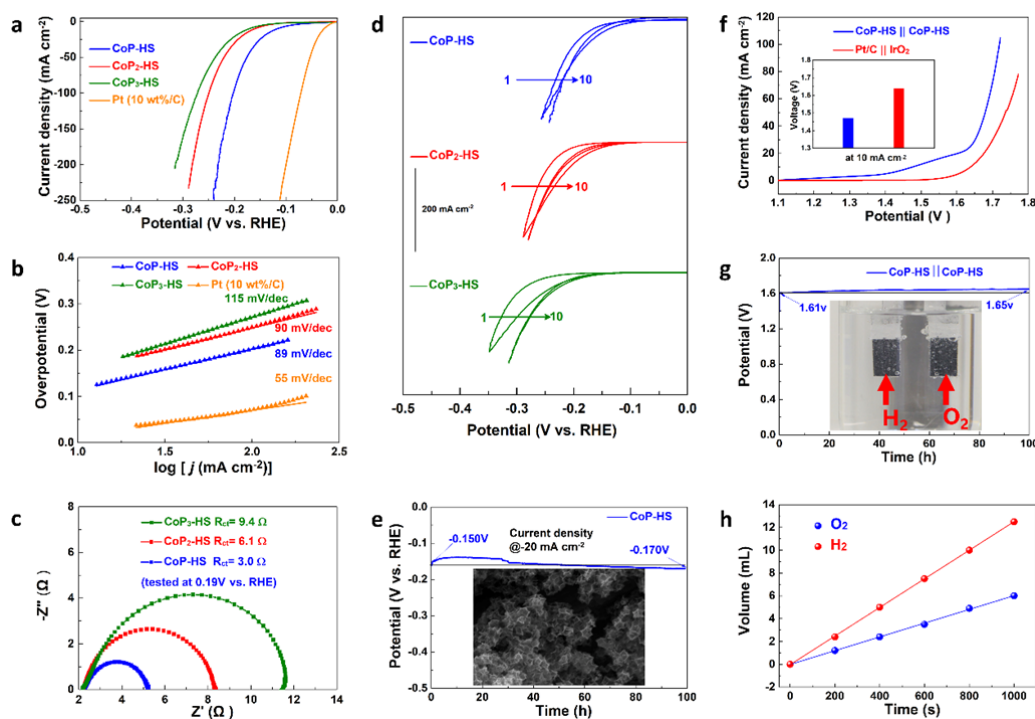
288 **Figure 4. (a)** The LSV curves of CoP-HS, CoP$_2$-HS, CoP$_3$-HS and Pt/C measured in 1.0 M KOH

289 toward HER at scan rate 10 mV/s. **(b)** The corresponding Tafel plots for the samples in 1.0 M

290 KOH. **(c)** Nyquist plots of CoP-HS, CoP$_2$-HS and CoP$_3$-HS in 1.0 M KOH. (All the tests were

291 taken on carbon paper). **(d)** The CV curves of CoP-HS, CoP$_2$-HS and CoP$_3$-HS measured in 1.0 M

292 KOH solution for 1st and 10th cycles at a scan rate 10 mV/s. **(e)** The chronopotentiometry curve

16

293 of CoP-HS at the current density of -20 mA cm^{-2} for 100 h in 1 M KOH. The inset in (e) is the

294 SEM image of CoP-HS after 100 h HER stability measurement in 1 M KOH. (f) Overall water

295 splitting performance based on the CoP‖CoP and Pt/C‖IrO$_2$ electrodes in 1 M KOH. The inset in (f)

296 is the potential of CoP‖CoP and Pt/C‖IrO$_2$ at a current density of -10 mA cm^{-2}. (g) Long term

297 durability test of CoP in the two-electrode electrolyzes at 20 mA cm^{-2} for overall water splitting.

298 The inset in (g) is optical image during the overall water splitting. (h) Amount of H$_2$ and O$_2$ as a

299 function of time.

300   On the contrary, the catalytic process of cobalt based phosphides for HER is

301 different from OER. Based on previous studies, the P sites in cobalt phosphides could

302 be the active site for HER. To investigate the HER activity of three cobalt phosphides,

303 LSV curves after CV scans in 1.0 M KOH were recorded at a scan rate of 10 mV/s,

304 and all the curves were IR corrected (**Figure 4a**). As expected, the HER activity of

305 bare carbon paper is negligible (**Figure S8a**), and the Pt/C exhibits the best activity

306 with an overpotential of 25 mV at the current density of -10 mA cm^{-2}. 116 mV is

307 required for the CoP-HS to achieve the current density of -10 mA cm^{-2}, which is much

308 lower than that of CoP$_2$-HS (159 mV) and CoP$_3$-HS (170 mV). The Tafel plots

309 derived from the LSV polarization curves are displayed to estimate the reaction

310 kinetics. As expected, the Tafel slope of commercial Pt/C is 34 mV dec^{-1} (**Figure 4b**),

311 which is consistent with the reported value.[34] The Tafel slope of CoP-HS, CoP$_2$-HS

312 and CoP$_3$-HS is 89, 90, and 115 mV dec^{-1}, respectively. According to literature, the

313 HER occurs through three different individual steps, which are named Volmer,

314 Heyrovsky, and Tafel reaction.[35] The Tafel values of three cobalt phosphides indicate

315 that a Volmer-Heyrovsky reaction, which happens on the surface of catalysts, is the

17

316 rate-determining step. Moreover, electrochemical impedance spectroscopy was used

317 to investigate the electron transfer kinetics during the HER process. As shown in

318 **Figure 4c**, the Nyquist plots of different catalysts are measured at -0.19 V. The inset

319 in **Figure 4c** displays the equivalent circuit model. The intersection of the plots on the

320 real axis represents the solution resistance (R_s) and the diameter of the semi-circle

321 represents the charge transfer resistance (R_{ct}) across the electrode-solution interface,

322 repectively.[36] CoP-HS possesses the smallest R_{ct} value.[37] The phase and

323 electrochemical stability of the three cobalt phosphides during HER are investigated

324 in the same way as in the OER experiments. Firstly, the CV curves of three cobalt

325 phosphides at the 1st, 3rd, 5th, and 10th cycles were conducted. As illustrated in

326 **Figure 4d&S9**, after 3 CV cycles, the CV curves of the three cobalt phosphides

327 display only minor changes, which indicates that three cobalt phosphides reach a

328 stable electrochemical state in a short period of time. Overall, CoP-HS is always

329 displaying the best HER performance in three cobalt phosphides. It could be

330 explained by XPS that the bonding energy of P 2p negatively shifted with the decrease

331 of P concentration in cobalt phosphides (CoP-HS <CoP_2-HS <CoP_3-HS), indicating

332 the enhanced electron occupation to improve the electron-donating ability.[29]

333 Chronopotentiometry was conducted to evaluate the stability of these catalysts. After

334 100 hours durability test, CoP retained good catalytic activity with a 17% decrease in

335 potential (**Figure 4e**). After 100 hours of OER, SEM, XPS, and SEM-EDX were used

336 to investigate the morphology, structure and composition of CoP-HS (**Figure**

337 **4e&S10**). As shown in the SEM images, the CoP-HS preserves its morphological

338   integrity (inset of **Figure 4e**). Based on the XPS results (**Figure S10a**), phosphorous

339   can be clearly detected after HER test, which is different to the situation for OER

340   (**Figure 3g**). Moreover, the chemical composition analyzed by SEM-EDS chemical

341   mapping shows that the atomic ratio of Co/P is close to 1.3 (**Figure S10b**), which

342   indicates the stability of CoP-HS during HER test in alkaline medium. All these

343   results prove that CoP-HS shown high stability for HER. Compared with recent

344   reports, the HER performance of CoP-HS is comparable or better than most cobalt

345   based HER electrocatalysts in alkaline solution (**Table S2**). In view of the stability of

346   the three cobalt phosphides in acid solution, the HER activity of CoP-HS, CoP$_2$-HS

347   and CoP$_3$-HS were also explored in 0.5 M H$_2$SO$_4$ (**Figure S11**). Similar results to the

348   HER in alkaline solution are achieved in that CoP-HS was still the best catalysts

349   (**Figure S12**) and comparable to other CoP catalysts reported in literature (**Table S3**).

350   The electrochemical stability of these three cobalt phosphides during HER in acid

351   solution were investigated via CV test at various cycles (**Figure S13**), and 100 hours

352   stability test at the current density of -20 mA cm^{-2} in 0.5 M H$_2$SO$_4$ (**Figure S14a**).

353   Finally, the high stability on phase structure of CoP-HS in acid solution was proven

354   via SEM, XPS, and SEM-EDS of the CoP-HS after 100 hours HER stability

355   measurement (**Figure S14b-d**).

356   According to the above results, the CoP-HS electrocatalyst was used as both

357   anode and cathode for water splitting in a two-electrode configuration in 1.0 M KOH

358   at 25°C. As shown in **Figure 4f**, a current density of 10 mA cm^{-2} is achieved at a

359   remarkably low cell voltage of 1.47 V, which is better than that of the benchmark

360   Pt/C||IrO$_2$ system with the same mass loading. Compared with literature, the water

361   splitting performance of CoP-HS is comparable or better than most of the cobaltbased

362   water splitting electrocatalysts in alkaline solution (**Table S4**). The long-term

363   operational stability of the CoP-HS||CoP-HS system was evaluated by

364   chronopotentiometry test at a current density of 20 mA cm^{-2}. After 100 h, almost no

365   degradation can be observed, indicating the stability of the CoP-HS||CoP-HS for

366   alkaline water electrolysis (**Figure 4g**). The H$_2$ and O$_2$ generated from the alkaline

367   electrolyzer were quantitatively collected by the water drainage method and displayed

368   in **Figure S15**. The volume–time curve in **Figure 4h** reveals a volume ratio of 2.07:1

369   for the collected H$_2$ to O$_2$, which approaches the theoretical 2:1 ratio for water

370   electrolysis. Based on the measured volume ratio, the Faradaic efficiency is estimated

371   to be ≈100% by considering the airtightness of the device. All these results

372   demonstrate that the prepared CoP-HS bifunctional catalyst is a promising candidate

373   catalyst for alkaline water electrolysis.
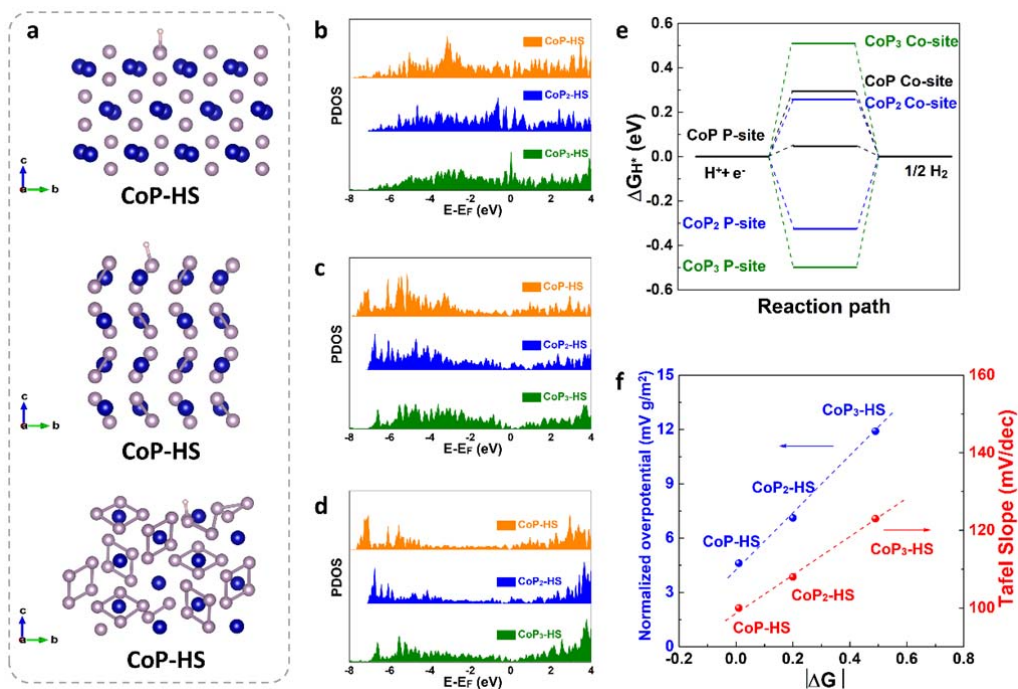
Figure 5. **(a)** Optimized configurations of CoP-HS, CoP$_2$-HS and CoP$_3$-HS for the DFT calculation. **(b)** Projected density of states (PDOS) plots of P 3p orbitals. **(c)** PDOS plots of P 3p orbitals in CoP-HS, CoP$_2$-HS and CoP$_3$-HS when H was adsorbed. **(d)** PDOS plots of H 1s orbitals in CoP-HS, CoP$_2$-HS and CoP$_3$-HS when H was adsorbed. **(e)** HER free energy changes of CoP-HS, CoP$_2$-HS and CoP$_3$-HS at P-sites and Co-sites. **(f)** The correlation between the HER free energy changes based on P-sites of CoP$_x$-HS and the normalized overpotential as well as Tafel slope.

In order to gain insights into the electrocatalytic HER activity of the CoP-HS, CoP$_2$-HS and CoP$_3$-HS, DFT calculations were performed. According to the XRD and TEM results, the selected configurations of CoP-HS, CoP$_2$-HS and CoP$_3$-HS are shown in **Figure 5a** based on stable facets. As P was determined as the active center in all three cobalt phosphides system, the difference of electronic structure on P of the parent CoP$_x$-HS were investigated via DFT (**Figure 5b**). As shown in the **Figure 5b**, it could be observed that the energy shift upwards with P composition increasing in

21

389 CoP$_x$-HS system, which indicates that CoP$_3$-HS has the strongest covalent interaction

390 between Co and P. The difference in electronic structure of CoP-HS, CoP$_2$-HS, and

391 CoP$_3$-HS can affect the electron transfer process during electrocatalytic reactions.

392 Moreover, the interaction effects on surface adsorbents of three cobalt phosphides

393 display the trend of CoP-HS <CoP$_2$-HS <CoP$_3$-HS, which means that CoP$_3$-HS has

394 the strongest H adsorption. After H adsorption, a significant rearrangement of

395 electrons in CoP$_x$-HS could be observed in P 3p (**Figure 5c**) compared with their

396 corresponding parent CoP$_x$-HS (**Figure 5b**). Similarly, CoP-HS is the best catalyst in

397 the CoP$_x$-HS for desorption process with the most negative position on electronic

398 distribution. The calculation results of PDOS of H 1s on three cobalt phosphides agree

399 well with the PDOS of P 3p (**Figure 5d**). When H is adsorbed on the surface, the P 3p

400 orbital shifts downwards in all three cobalt phosphides, but especially in CoP-HS,

401 leading to more filled antibonding states of the H 1s orbital and hence resulting in a

402 weakened H-P bond, which is beneficial for the desorption of H$_2$. To understand the

403 effect of changes from the electronic structure in three cobalt phosphides on HER, the

404 free energy of hydrogen chemisorption on the surface of the selected CoP-HS,

405 CoP$_2$-HS and CoP$_3$-HS configurations were calculated by DFT. Details of the possible

406 configurations of CoP$_x$-HS are given in **Figure S16-18,** with the corresponding

407 calculated ΔG_{H*} values in **Figure S19**. As shown in **Figure 5e**, the final ΔG_{H*} values

408 of CoP$_x$-HS from optimized configurations on Co- and P-sites are 0.24 eV and 0.01

409 eV for CoP-HS, 0.23 eV and -0.32 eV for CoP$_2$-HS and 0.44 eV and -0.50 eV for

410 CoP$_3$-HS, respectively. Generally speaking, a smaller ΔG_{H*} will translate into a better

411 HER activity.[38] To understand the intrinsic correlation between P-sites/Co-sites in

412 CoP$_x$-HS and HER activity, the normalized LSV curves of CoP$_x$-HS in 1.0 M KOH

413 toward HER were calculated (**Figure S20**). As shown in **Figure 5f**, the calculated

414 ΔG_{H*} based on P-sites of CoP$_x$-HS follows a quite similar trend with the normalized

415 overpotential and Tafel slope, indicating the important role of P-sites on the surface of

416 CoP$_x$ for the HER process. Meanwhile, no significant correlation exists between

417 Co-sites and the HER performance (normalized overpotential and Tafel slope) for the

418 CoP$_x$-HS system (**Figure S21**). Therefore, it is likely that the surface

419 absorption/desorption capacity on P-sites of CoP$_x$-HS is the intrinsic rate-determining

420 factor for the HER process.

3. Conclusions

422   ZIF-67 MOF was used to synthesize porous CoP-HS, CoP$_2$-HS and CoP$_3$-HS

423 nanocages. As confirmed by experimental results, the cobalt phosphides work as

424 pre-catalyst for OER rather than as the active materials. After cycling in alkaline

425 solution, the near surface region of all three Co-phosphides transformed to

426 oxyhydroxide, resulting in identical OER performance after cycling. On the contrary,

427 the different cobalt phosphides exhibited a high stability and clear different catalytic

428 activities for the HER. CoP-HS nanocages showed the best catalytic activity for HER

429 with an overpotential of -116 mV at a current density of -10 mA cm^{-2} in 1 M KOH.

430 Based on density functional theory (DFT) calculations, the calculated ΔG_{H*} on P-sites

431 were lower than those on Co-sites in CoP$_x$-HS system. Moreover, the calculated ΔG_{H*}

432 based on P-sites of CoP-HS follows a quite similar trend with the normalized

433 overpotential and Tafel slope, indicating the important role of P-sites for the HER

434 process. Moreover, no significant correlation between Co-sites and the HER

435 performance (overpotential and Tafel) for all the CoP_x-HS was found. This indicates

436 that the P-sites are probably the catalytically active sites for HER. When

437 CoP-HS//CoP-HS were used as bifunctional catalysts for water splitting in a cell

438 device, a current density of 10 mA cm^{-2} is achieved at a remarkably low cell voltage

439 of 1.47 V, which is one of the best bifunctional catalysts among the once reported in

440 literature. This excellent electrochemical performance of CoP-HS for overall water

441 splitting is derived from the hollow structure and high activity of P-sites in CoP-HS.

442 These results shed new light on the design and development of other transition metal

443 phosphides materials for water splitting.

Author Contributions

463 W. Z and N. H conceived and designed the research, coordinated the work, made the

464 visualization of the experiment results, performed the mechanism analysis. J. A and X.

465 H conducted TEM and performed the corresponding data analysis. W. Z, X. Z and M.

466 X conducted the BET and XPS, and W. Z performed the data analysis. C. Z conducted

467 the first principles calculation, W. Z and N. H performed the data analysis. W. G, S. X

468 and Z. Z conducted the SEM and XRD, W. Z and N. H performed the data analysis. P.

469 S and K. W assisted in the electrochemistry test. W. Z wrote the manuscript, and C. Z,

470 X. Z, J. L and J. F assisted in revising the manuscript. All co-authors contributed to

471 this work.

Note and references

473 1.   Tiwari, J. et al. Multicomponent electrocatalyst with ultralow Pt loading and high hydrogen

474   evolution activity. *Nat Energy* **3**, 773-782 (2018).

475

476   2.   Turner, J. Sustainable hydrogen production. *Science* **305**, 972-974 (2004).

477

478   3.   Sultan, S. et al. Superb water splitting activity of the electrocatalyst $Fe_3Co(PO_4)_4$ designed
479   with computation aid. *Nat. Commun.* **10**, 1-9 (2019).

480

481   4.   Roger, I., Shipman, M. & Symes, M. Earth-abundant catalysts for electrochemical and
482   photoelectrochemical water splitting. *Nat. Rev. Chem.* **1**, 1-13 (2017).

483

484   5.   Wang, X., Li, W., Xiong, D., Petrovykh, D, & Liu, L. Bifunctional Nickel Phosphide
485   Nanocatalysts Supported on Carbon Fiber Paper for Highly Efficient and Stable Overall Water
486   Splitting. *Adv. Funct. Mater.* **26**, 4067-4077 (2016).

487

488   6.   Tan, Y. et al. Versatile nanoporous bimetallic phosphides towards electrochemical water
489   splitting. *Energy Environ. Sci.* **9**, 2257-2261 (2016).

490

491   7.   Tang, B., Yang, X., Kang, Z. & Feng, L. Crystallized $RuTe_2$ as unexpected bifunctional
492   catalyst for overall water splitting. *Appl. Catal. B-Environ.* **278**, (2020).

493

494   8.   Ling, C., Shi, L., Ouyang, Y., Zeng, X. & Wang, J. Nanosheet Supported Single-Metal Atom
495   Bifunctional Catalyst for Overall Water Splitting. *Nano Lett.* **17**, 5133-5139 (2017).

496

497   9.   Wang, H. et al. Bifunctional non-noble metal oxide nanoparticle electrocatalysts through
498   lithium-induced conversion for overall water splitting. *Nat. Commun.* **6**, 7261 (2015).

499

500   10.   Prabhakaran, S., Balamurugan, J., Kim, N. & Lee, J. Hierarchical 3D Oxygenated Cobalt
501   Molybdenum Selenide Nanosheets as Robust Trifunctional Catalyst for Water Splitting and
502   Zinc–Air Batteries. *Small* **16**, 2000797 (2020).

503

504   11.   Masa, J. et al. Amorphous cobalt boride (Co_2B) as a highly efficient nonprecious catalyst for
505   electrochemical water splitting: oxygen and hydrogen evolution. *Adv. Energy. Mater.* **6**,
506   1502313 (2016).

507

508   12.   Zhou, H. et al. Water splitting by electrolysis at high current densities under 1.6 volts. *Energy*
509   *Environ. Sci.* **11**, 2858-2864 (2018).

510

511   13.   Han, N., Liu, P., Jiang, J., Ai, L., Shao, Z. & Liu, S. Recent advances in nanostructured metal
512   nitrides for water splitting. *J Mater. Chem. A* **6**, 19912-19933 (2018).

513

514   14.   Joo, J., Kim, T., Lee, J., Choi, S. & Lee, K. Morphology controlled metal sulfides and
515   phosphides for electrochemical water splitting. *Adv. Mater.* **31**, 1806682 (2019).

516

517   15.   Ryu, J., Jung, N., Jang, J., Kim, H. & Yoo, S. In Situ Transformation of Hydrogen-Evolving

CoP Nanoparticles: Toward Efficient Oxygen Evolution Catalysts Bearing Dispersed Morphologies with Co-oxo/hydroxo Molecular Units. *ACS Catal.* **5**, 4066-4074 (2015).

16. Wu, R. et al. A Janus Nickel Cobalt Phosphide Catalyst for High-Efficiency Neutral-pH Water Splitting. *Angew Chem. Int. Ed.* **57**, 15445-15449 (2018).

17. Pan, Y. et al. Core–shell ZIF-8@ ZIF-67-derived CoP nanoparticle-embedded N-doped carbon nanotube hollow polyhedron for efficient overall water splitting. *J. Am. Chem. Soc.* **140**, 2610-2618 (2018).

18. Wang, Q. et al. Mo-doped Ni_2P hollow nanostructures: highly efficient and durable bifunctional electrocatalysts for alkaline water splitting. *J. Mater. Chem. A* **7**, 7636-7643 (2019).

19. Du, C., Yang, L., Yang, F., Cheng, G., & Luo, W. Nest-like NiCoP for Highly Efficient Overall Water Splitting. *ACS Cataly* **7**, 4131-4137 (2017).

20. Zhang, H., Zhou, W., Dong, J., Lu, X, & Lou, X. Intramolecular electronic coupling in porous iron cobalt (oxy)phosphide nanoboxes enhances the electrocatalytic activity for oxygen evolution. *Energy Environ. Sci.* **12**, 3348-3355 (2019).

21. Hu, E., Feng, Y., Nai, J., Zhao, D., Hu, Y. & Lou, X. Construction of hierarchical Ni–Co–P hollow nanobricks with oriented nanosheets for efficient overall water splitting. *Energy Environ. Sci.* **11**, 872-880 (2018).

22. Liang, Z. et al. Fabrication of hollow CoP/TiO_x heterostructures for enhanced oxygen evolution reaction. *Small* **16**, 1905075 (2020).

23. Qiu, B. et al. Fabrication of Nickel-Cobalt Bimetal Phosphide Nanocages for Enhanced Oxygen Evolution Catalysis. *Adv. Funct. Mater.* **28**, (2018).

24. He, P., Yu, X. & Lou, X. Carbon-Incorporated Nickel-Cobalt Mixed Metal Phosphide Nanoboxes with Enhanced Electrocatalytic Activity for Oxygen Evolution. *Angew Chem. Int. Ed. Engl* .**56**, 3897-3900 (2017).

25. Guan, C. et al. Hollow Mo-doped CoP nanoarrays for efficient overall water splitting. *Nano Energy* **48**, 73-80 (2018).

26. Zhang, J., Hu, H., Li, Z. & Lou, X. Double-Shelled Nanocages with Cobalt Hydroxide Inner Shell and Layered Double Hydroxides Outer Shell as High-Efficiency Polysulfide Mediator for Lithium-Sulfur Batteries. *Angew Chem. Int. Ed.* **55**, 3982-3986 (2016).

27. Zha, Q., Xu, W., Li, X. & Ni, Y. Chlorine-doped alpha-Co(OH)$_2$ hollow nano-dodecahedrons prepared by a ZIF-67 self-sacrificing template route and enhanced OER catalytic activity.

562   *Dalton Trans.* **48**, 12127-12136 (2019).

563

564   28.   Cao, H. et al. Flower-like CoP microballs assembled with (002) facet nanowires via precursor

565   route: Efficient electrocatalysts for hydrogen and oxygen evolution. *Electrochim. Acta* **259**,

566   830-840 (2018).

567

568   29.   Yan, L. et al. Metal-Organic Frameworks Derived Nanotube of Nickel-Cobalt Bimetal

569   Phosphides as Highly Efficient Electrocatalysts for Overall Water Splitting. *Adv. Funct. Mater.*

570   **27**, (2017).

571

572   30.   Jamesh, M. & Sun, X. Recent progress on earth abundant electrocatalysts for oxygen

573   evolution reaction (OER) in alkaline medium to achieve efficient water splitting – A review. *J.*

574   *Power Sources* **400**, 31-68 (2018).

575

576   31.   Mabayoje, O., Shoola, A., Wygant, B. & Mullins, C. The Role of Anions in Metal

577   Chalcogenide Oxygen Evolution Catalysis: Electrodeposited Thin Films of Nickel Sulfide as

578   "Pre-catalysts". *ACS Energy Lett.* **1**, 195-201 (2016).

579

580   32.   Yu, F. et al. Three-Dimensional Nanoporous Iron Nitride Film as an Efficient Electrocatalyst

581   for Water Oxidation. *ACS Catal.* **7**, 2052-2057 (2017).

582

583   33.   Ye, S., Shi, Z., Feng, J., Tong, Y. & Li, G. Activating CoOOH Porous Nanosheet Arrays by

584   Partial Iron Substitution for Efficient Oxygen Evolution Reaction. *Angew Chem. Int. Ed.* **57**,

585   2672-2676 (2018).

586

587   34.   Xiao, P. et al. Molybdenum phosphide as an efficient electrocatalyst for the hydrogen

588   evolution reaction. *Energy Environ. Sci.* **7**, 2624-2629 (2014).

589

590   35.   Shinagawa, T., Garcia-Esparza, A. & Takanabe, K. Insight on Tafel slopes from a microkinetic

591   analysis of aqueous electrocatalysis for energy conversion. *Sci. Rep.* **5**, 13801 (2015).

592

593   36.   Zhang, X. et al. From rational design of a new bimetallic MOF family with tunable linkers to

594   OER catalysts. *J. Mater. Chem. A* **7**, 1616-1628 (2019).

595

596   37.   Cao, E. et al. Boron-Induced Electronic-Structure Reformation of CoP Nanoparticles Drives

597   Enhanced pH-Universal Hydrogen Evolution. *Angew Chem. Int .Ed.* **59**, 4154-4160 (2020).

598

599   38.   Huang, X., Xu, X., Li, C., Wu, D., Cheng, D. & Cao, D. Vertical CoP Nanoarray Wrapped by

600   N,P Doped Carbon for Hydrogen Evolution Reaction in Both Acidic and Alkaline Conditions.

601   *Adv. Energy Mater.* **9**,   (2019).

602

603

604